Received: 20 February 2023 | Accepted: 8 June 2023

DOI: 10.1002/cnl2.79

RESEARCH ARTICLE

Carbon Neutralization WILEY

Biochar-based interfacial evaporation materials derived from lignosulfonate for efficient desalination

Shilin Chen | **Lan Sun** | **Yuqing Huang** | **Dongjie Yang** | **Mingsong Zhou** | **Dafeng Zheng**

School of Chemistry and Chemical Engineering, South China University of Technology, Guangzhou, China

Correspondence
Dongjie Yang and Dafeng Zheng, School of Chemistry and Chemical Engineering, South China University of Technology, Guangzhou 510640, China.
Email: cedjyang@scut.edu.cn and zhengdf@scut.edu.cn

Funding information
Natural Science Foundation of Guangdong Province, Grant/Award Number: 2022A1515010757; National Key Research and Development Plan, Grant/Award Number: 2018YFB1501503; Science and Technology Program of Guangdong, Grant/Award Number: 2020B1111380002; National Natural Science Foundation of China, Grant/Award Number: 22178127

Abstract

The solar-driven interfacial evaporation has attracted great attention for the purpose of alleviating freshwater shortage. Lignosulfonate (LS), a main byproduct of sulfite pulping processes, is an abundant natural resource but has not been reasonably utilized. To mitigate the above problems, biochar-based interfacial evaporators derived from LS for solar steam generation were studied in this paper. First, LS was used as a raw material for fabricating carbon materials by carbonization to construct LS-derived carbon (CLS). Meanwhile, LS-derived porous carbon (PCLS) in the presence of $CaCO_3$ as the activator was also prepared. Next, the two biochar powders, as solar absorbers, were crosslinked with polyvinyl alcohol to prepare the interfacial evaporation materials (PVA@PCLS and PVA@CLS). The open porous structure facilitated the capillary effect and water transport to the evaporator surface. It was also found that the light absorption of the materials could reach more than 97% in the 250–2500 nm range. Moreover, the water evaporation rate and the solar-to-vapor conversion efficiency of PVA@PCLS and PVA@CLS were 2.33, 1.82 $kg\,m^{-2}\,h^{-1}$, and 83.7%, 69.3% respectively under 1 sun (1 $kW\,m^{-2}$) irradiation. The solar-to-vapor conversion efficiency of PVA@PCLS was much increased after the carbonization of LS. In addition, the material cost of PVA@PCLS is only \$38.3/kg due to the low price of LS. Therefore, this work provides an economic and efficient strategy for solar-driven desalination and a possible way for the high-value utilization of lignin.

KEYWORDS
interfacial evaporation, light absorption, lignosulfonate, porous biochar, solar-to-vapor conversion efficiency

Highlights

- Biochar was produced through the carbonization of lignosulfonate.
- PCLS has smaller particle size and larger multistage pore.

Shilin Chen and Lan Sun contributed equally to this study.

- Green, efficient interfacial evaporation materials derived from biochar were prepared by simple processes.
- Among the three interfacial evaporation materials, PVA@PCLS has the largest water evaporation rate and solar-to-vapor conversion efficiency.
- The material cost of PVA@PCLS is rather low.

1 | INTRODUCTION

With the growing development of modern society, the demand for freshwater is increasing. Although three-quarters of the earth's surface is covered by water, less than 3% of it is available for plants, animals, and human life activities.[1–3] Even so, fresh water is unevenly distributed across the planet, resulting in inadequate water supplies in many areas. It is supposed by the World Health Organization (WHO) that about half of the world's population will face a lack of freshwater resources by 2050.[4,5]

As is well known, desalination from seawater is one of the most important methods to solve the shortage of freshwater.[6–8] Solar energy is safe, low-cost, and green compared to other energy sources such as wind, tide, and nuclear power.[9,10] In the early days, seawater was desalinated by concentrating sunlight and heating it to generate water vapor.[11] However, this method often has the disadvantage of low efficiency and has not been widely used.

In recent years, solar-driven interfacial evaporation has been proposed by researchers as a promising alternative to traditional solar heating evaporation due to its higher energy conversion efficiency. Currently, a variety of solar thermal conversion materials are used for interfacial evaporation, such as graphene,[12] carbon dots,[13] semiconductors,[14] and plasmonic metal.[15] However, their mass production for practical applications is impeded by costly raw materials, complex preparation processes, and nonbiodegradability.[16–18] Low cost, ease of operation, and high stability are the keys to the broad application of interfacial evaporation materials. Therefore, it has become a hotspot for researchers to design a cheap interfacial evaporation material with a high evaporation rate and facile preparation process.

Industrial lignin is a large by-product in the pulping and cellulosic ethanol industries (annual output of approximately 70 million tons),[19] with low prices and abundant sources. However, most lignin has not been reasonably utilized until now, resulting in a huge waste of resources.[20] Lignin has an abundant aromatic ring structure, aliphatic, aromatic hydroxyl, and quinone groups, which enables it with strong π–π stacking, and can promote nonradiative migration and trigger photothermal conversion.[21] Moreover, lignin contributes 30 wt% of the biochar content on Earth, is an economical and sustainable substrate for aerogel production.[22] Based on our previous findings, lignin and its derivatives can be used as starting materials to yield carbon materials with diverse morphologies and porous structures by carbonization or activation,[23] which can be employed as an ideal carbon-based photothermal material. Nowadays, with an increase in scarce resources, it is of great significance to achieve the goal of carbon neutrality by realizing the high-value utilization of lignin and making use of solar energy for interfacial evaporation to produce freshwater.

Therefore, in this work, we prepared two kinds of biochar particles by carbonization of lignosulfonate (LS), then construct biochar-based interfacial evaporation materials by using the prepared biochar and polyvinyl alcohol (PVA). The performance of evaporators in desalination was investigated. This work will provide a possible way for high-value utilization of lignin and a simple strategy for designing a green solar-driven interfacial evaporation aerogel.

2 | MATERIALS AND METHODS

2.1 | Materials

Sodium LS is a by-product of sulfite pine pulping processes, with an average molecular weight of 23,000, which is provided by Youbang Chemical Ltd.

PVA is in chemical purity, with an average molecular weight of 15,000 and alcoholysis degree of 87%–89.0% (molar fraction), which is purchased from Aladdin Reagent Ltd.

Glutaraldehyde (GA [50 wt% in water]), HCl, $CaCl_2$, and K_2CO_3 are all in chemical purity and are purchased from Maclin Co. Ltd.

2.2 | Experiments

2.2.1 | Preparation of biochar derived from LS

Sodium LS (6 g) was placed in a tubular furnace with nitrogen as the protective gas, and the carbonization

product was obtained after a constant temperature of 700°C for 2 h.

The resulting carbonized product was stirred in 1 M HCl solution for 6 h and washed with deionized water to remove the soluble impurities, and then dried in an oven at 80°C for 24 h to obtain the carbon powder. The powder was then ground in an agate mortar and screened with 500 mesh stainless steel to obtain LS-based biochar (CLS).

Porous LS-based biochar powder (PCLS) was prepared according to our previous research method with a slight modification.[24] The other kind of LS-based porous biochar was prepared via the following strategy. First, 6 g of sodium LS and 2.2 g of $CaCl_2$ were dissolved in 60 mL of deionized water and stirred for 2 h until completely dissolved. 2.8 g of K_2CO_3 was next dissolved in 30 mL of deionized water and the K_2CO_3 solution was slowly added to the above solution under magnetic stirring until precipitates were generated. The obtained solids were centrifuged (10,000 rpm, 5 min) and dried in an oven at 80°C for 24 h. The dried composite was then ground and placed in a horizontal tubular furnace, heated to 700°C at the rate of 5°C/min for 2 h in an N_2 atmosphere. Subsequently, the as-obtained product was washed using 1 M HCl solution for 6 h to remove the template and other impurities, followed by being rinsed with deionized water until the carbonized products reached neutral and dried in an oven overnight at 80°C. The final biochar was labeled as PCLS.

2.2.2 | Preparation of biochar-based interfacial evaporation materials

One gram of PVA was dissolved in 10 mL of deionized water, and then 125 μL of 50% GA solution was added. The mixture was stirred in a 500 W ultrasonic cell grinder for 10 min until the solid was completely dissolved. Then 0.1 g of biochar powder was added to the mixture, and stirred for 5 h, followed by 0.5 mL of 1.2 M HCl solution. After that, the mixture was poured into a mold to gel at room temperature for 12 h, then the hydrogel was repeatedly frozen and thawed 10 times in the freezer at −28°C, and finally freeze-dried at −48°C for 48 h to obtain the biochar-based interfacial evaporation aerogel. Among them, the interfacial evaporation material doped with CLS was labeled as PVA@CLS, and that doped with PCLS was labeled as PVA@PCLS. For comparison, an interfacial evaporation material doped with pristine LS was also prepared and denoted as PVA@LS.

2.3 | Characterization

The morphology of samples were characterized by scanning electron microscopy (FE-SEM SU-8220; HITACHI). The pore structure was investigated using an environmental scanning electron microscope (Quanta 200; FEI) and an automatic mercury porosimeter (Autopore IV 9500). The water contact angle was detected with a contact angle meter (DSA100; KRUSS). The mechanical properties of the samples were studied using a universal testing machine (CMT4204; Mets), and all aerogel samples were tested at least in triplicate. The Raman spectra of samples were recorded by a Raman spectrometer (HJY LabRAM Aramis). The FTIR spectra were obtained at room temperature using a Fourier transform infrared spectrometer (Nicolet iS50; Thermo Fisher Scientific) in the range of 4000–400 cm^{-1}. The element compositions of the samples were measured by an elemental analyzer (Elementar Vario EL cube). The light absorption was determined by the UV–Vis–NIR spectrometer (PerkinElmer Lambda 950). Thermal conductivity of the samples was tested using a conductometer (Hot Disk TPS 2500) at room temperature. Differential scanning calorimetry (DSC) experiment was conducted by a thermal gravimetric analyzer (TG 209 F3 Tarsus). The concentrations of ions in water samples were tracked by an inductively coupled plasma mass spectrometer (ICP-MS 7700; Agilent). The surface area of CLS and PCLS were estimated using BET (Brunauer-Emmett-Teller, Quantachrome NOVA 2200), and the pore size distribution was collected by density functional theory model.

2.4 | Solar steam generation experiments

All the solar steam generation experiments were conducted using the same solar simulator (PLS-SXE300BF) with an AM 1.5 G filter. An infrared camera (FLIR A315) was used to monitor the surface temperature of the solar evaporator. The light intensity was measured using an optical power meter (CEL-NP2000) before each experiment. Experimental data was recorded by a computer (RS232) during evaporation. The exposed area under irradiation was about 2.25 cm^{-2} with a thickness of ~10 mm. The room temperature was 26 ± 2°C and the ambient humidity was about 55%.

2.5 | Calculation of solar-to-vapor conversion efficiency

In the process of sunlight irradiating the surface of the material, the material first absorbs sunlight and converts it into heat energy, and then transfers the heat energy to some water molecules in the sample, thereby causing the evaporation of water. The solar-to-vapor conversion efficiency is calculated according to Equation (1):

$$\eta = \frac{mH_v}{C_{\text{opt}} q_i}, \tag{1}$$

where m refers to the evaporation rate of water per unit area and unit time (the total rate measured minus the evaporation rate in darkness under natural conditions) ($\text{kg m}^{-2}\,\text{h}^{-1}$); H_v is the enthalpy of water evaporation in the gel network (kJ g^{-1}); C_{opt} is the optical concentration on the surface of the interfacial evaporation material; q_i represents the radiant flux under 1 sun, usually equal to $1\,\text{kW m}^{-2}$.

2.6 | Calculation of equivalent evaporation enthalpy

Dark experiments and DSC measurements were used to calculate the energy consumption for evaporation of pure water and water in the fabricated solar evaporators. For dark experiments, the specific method is as follows:

Water, wet interfacial evaporation material, and supersaturated potassium bicarbonate solution with the same surface area were placed (the humidity was stabilized at about 45%) in an airtight container under atmospheric pressure and at 25°C. The equivalent evaporation enthalpy (ΔH_{equ}) is calculated by Equation (2):

$$U_{\text{in}} = \Delta H_{\text{vap}} \times m_0 = \Delta H_{\text{equ}} \times m_g, \tag{2}$$

where U_{in} is the input equivalent total energy; ΔH_{vap} is the evaporation enthalpy of pure water at room temperature (25°C) ($2.436\,\text{kJ g}^{-1}$); m_0 is the mass change before and after the evaporation of pure water (kg); ΔH_{equ} is the equivalent evaporation enthalpy of water in the gel network formed by the interfacial evaporation material; m_g is the mass change (kg) of the water in the interfacial evaporation material before and after evaporation.

The second is the DSC experiment. To demonstrate the reduction of evaporation enthalpy of water in interfacial evaporation material, DSC was used to measure the evaporation enthalpy of pure water and water in the gel network of the interfacial evaporation material. The DSC tests were carried out under N_2 flow (50 mL/min) from 20°C to 200°C with a heating rate of 5°C/min.

3 | RESULTS AND DISCUSSION

3.1 | Structural characterization of biochar derived from LS

To better understand the size and structure of two kinds of biochar powder (CLS and PCLS), the microstructures were evaluated by SEM, as shown in Figure 1a–d. CLS appears irregularly granular with a relatively flat and smooth surface (Figure 1d). However, after template activation, the obtained PCLS showed a pompon-like structure with loose surface (Figure 1b). The internal structure of PCLS and CLS were shown in Figure 1e–h. The PCLS particles have well-developed pore structures and uniform pore size distribution. Except for some irregular macropores, most of the pores are mesopores and micropores, and the mesopores obviously account for the main proportion. Since template activation occurs both internally and externally, PCLS particles have cellular pore networks, which also make PCLS particles appear fluffy and porous. Due to the porous structure inside the PCLS particles, the effective refractive index of the material is reduced, thus reducing the reflection of light. In addition, these porous structures can realize light capture and multiple scattering/reflection to achieve excellent solar energy absorption.[25,26] For CLS, its cross-section is smooth and there are no pores, revealing that direct carbonization of LS at 700°C could not form loose pores in the interior.

The nanopore properties of CLS and PCLS were also characterized by N_2 adsorption/desorption method. Figure 2a,b shows the nitrogen adsorption–desorption isotherms and pore size distribution of CLS and PCLS. The surface area of CLS was found to be $9.77\,\text{m}^2/\text{g}$, and the total pore volume of $0.008\,\text{cm}^3/\text{g}$. By comparison, the specific surface area and total pore volume of PCLS are $486.35\,\text{m}^2/\text{g}$ and $0.527\,\text{cm}^3/\text{g}$, which are larger than CLS. Importantly, its mesopore volume reaches $0.403\,\text{cm}^3/\text{g}$, taking up 76.5% of total pore volume. The results show that the nanosize pores of PCLS are more abundant than those of CLS, which further confirms the microstructure shown in Figure 1.

The graphitization degree of two biochar samples were also examined by Raman spectrum shown in Figure 2c. It can be clearly observed that there were two strong peaks at 1348 and $1599\,\text{cm}^{-1}$, corresponding to the D-band and G-band, respectively. Generally

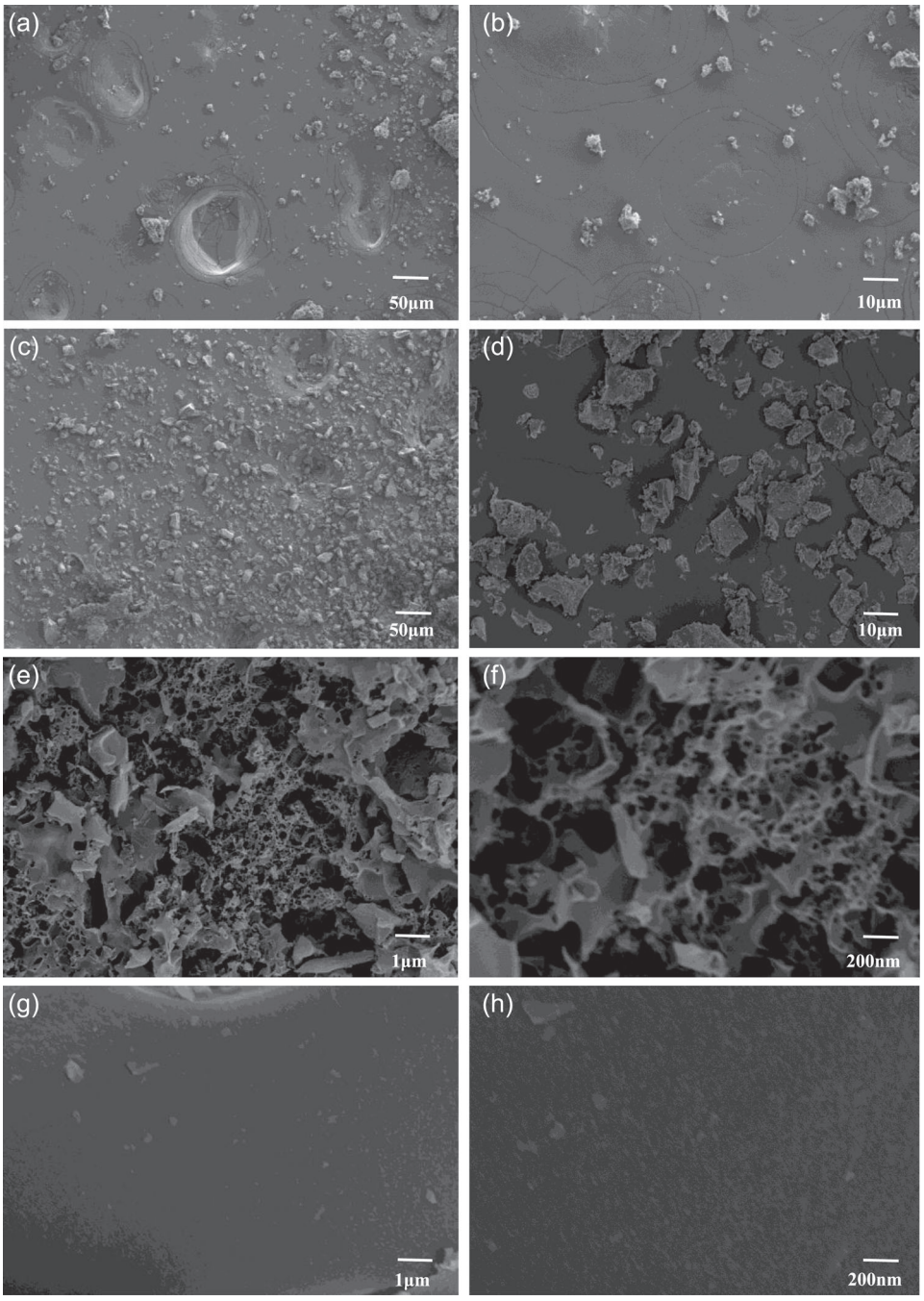

FIGURE 1 SEM images of external morphology of PCLS (a, b) and CLS (c, d); internal structure of PCLS (e, f) and CLS (g, h). LS, lignosulfonate; PCLS, porous LS-based biochar powder; SEM, scanning electron microscopy.

speaking, the D-band represents the disordered band related to the defective carbon atoms, indicating the defective graphite structure, while the G-band represents the ordered band of the carbon atoms hybridized in the form of sp^2, which is characteristic of the graphite crystal. It is well known that the intensity ratio of I_D/I_G can be used to estimate the graphitization degree of the carbon materials.[27] The higher the ratio is, the lower the graphitization degree of the carbon materials is, and the more disordered the structure will be. The calculated I_D/I_G values of CLS and PCLS are 0.96 and 1.02, respectively. This indicates that if the template is used in the carbonization process, the lattice defects of carbonized particles will increase, and the graphitization degree will also increase. This graphene-like structure can effectively absorb solar energy, and then achieve efficient photothermal conversion through energy-level transition and lattice vibration.

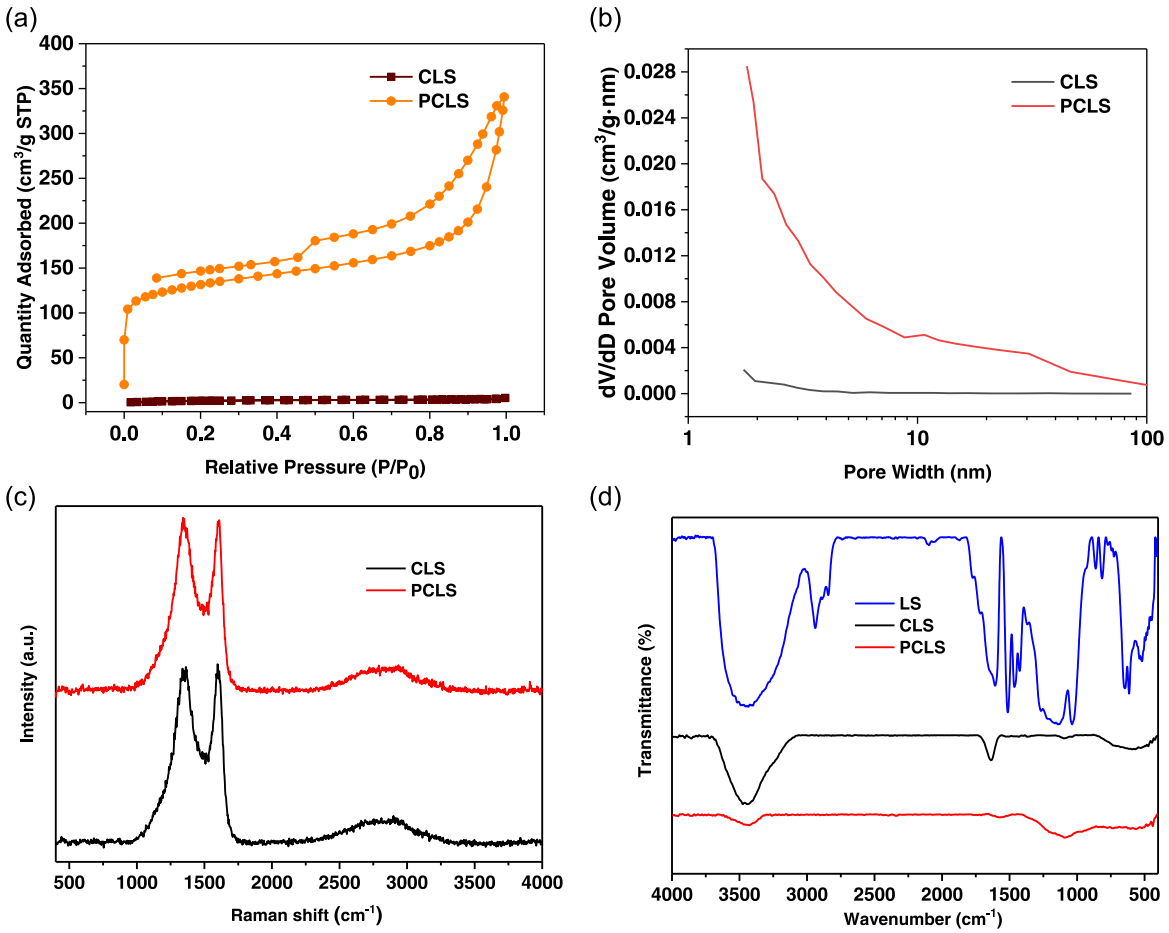

FIGURE 2 (a) Nitrogen adsorption–desorption isotherms; (b) DFT pore size distribution; (c) Raman spectra of PCLS and CLS; (d) FT-IR spectra of LS, CLS, and PCLS. DFT, density functional theory; FT-IR, Fourier-transform infrared spectroscopy; PCLS, porous LS-based biochar powder.

To determine the functional groups in the carbon powder, Fourier transform infrared spectroscopy (FTIR) of LS, CLS and PCLS were tested, and the results are shown in Figure 2d. For LS, the wide and strong characteristic absorption peak at 3439 cm^{-1} corresponds to the stretching vibration of the O–H bond,[28–30] the peak at 1521 cm^{-1} is ascribed to the stretching vibration of the benzene ring in LS, and the characteristic bands at 1685 cm^{-1} are assigned to carbon–oxygen double bond (C=O) vibrations.[31] The peak around 2940 cm^{-1} belongs to the stretching vibration of C–H bonds in $-CH_3$, whereas the peak at 2850 cm^{-1} is attributed to stretching vibrations of C–H bonds in $-OCH_3$. These two bands almost disappear in the spectra of the carbonized samples. For CLS and PCLS, there is also a stretching vibration peak of the hydroxyl group (–OH) at 3439 cm^{-1}. Compared with LS, the absorption peak intensity of the functional groups in CLS and PCLS is significantly reduced, especially the hydroxyl group, indicating that these functional groups are lost by pyrolysis. The hydrophilicity of CLS and PCLS decreases with the reduction of hydrophilic functional groups.

3.2 | Morphology and characterization of biochar-based interfacial evaporation materials

In the process of photothermal evaporation, the overflow of water and steam requires lots of channels in the evaporator. The structure of the interfacial evaporation materials was tested. From Figure 3b,c, it can be clearly seen that CLS and PCLS were well dispersed and embedded in the surface and framework, and the surface biochar was very irregular, with many depressions and bulges, so the solar light absorption would be enhanced compared with the smooth surface.[32]

Figure 3d–f presents SEM images of the internal structure. All three materials have multilevel honeycomb-like porous structures inside. These micro-structures were critical for solar radiation capture as they

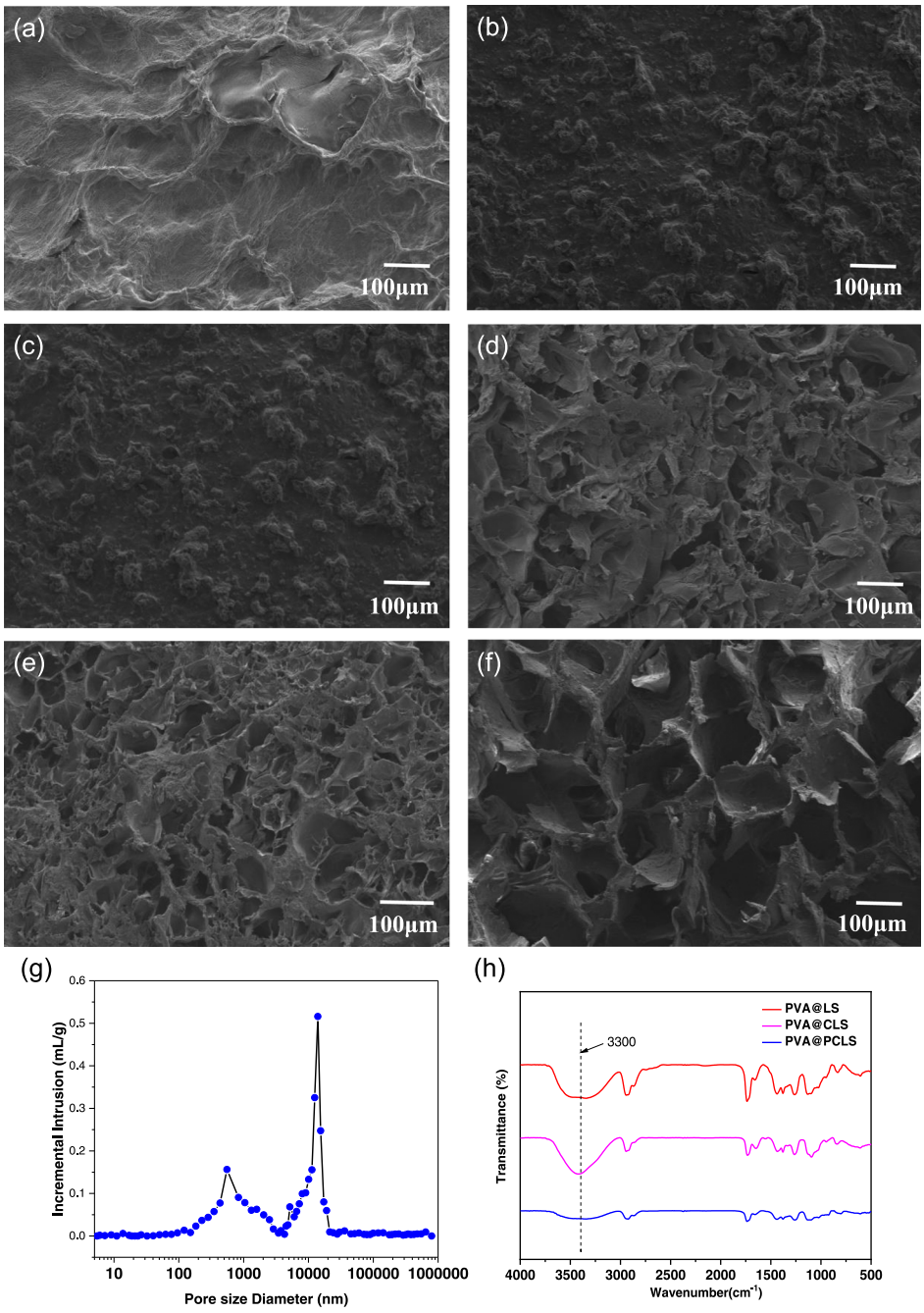

FIGURE 3 SEM images of the surface of interfacial evaporation materials (a) PVA@LS, (b) PVA@CLS, and (c) PVA@PCLS; The internal morphology of interfacial evaporation materials (d) PVA@LS, (e) PVA@CLS, and (f) PVA@PCLS; (g) Pore size distribution diagram of PVA@PCLS tested by mercury injection; (h) FT-IR spectra of PVA@LS, PVA@CLS, and PVA@PCLS. LS, lignosulfonate; PCLS, porous LS-based biochar powder; SEM, scanning electron microscope.

allowed solar light to reflect many times within the material. Besides, this multilevel structure can not only lock the incident light in the material but also be conducive to the overflow of steam and the transportation of water in the process of photothermal evaporation.

The porous structure of PVA@PCLS was tested by the mercury intrusion method further, as illustrated in Figure 3g. It can be seen in the pore distribution characteristic curve that the pore diameter of PVA@PCLS ranges from 5 nm to 100 μm. That is, nano and micron pores with different diameters are distributed inside PVA@PCLS. As light passes through this porous structure, it undergoes multiple reflections on the pore wall to maximize light absorption.[25]

The FTIR spectra of PVA@LS, PVA@CLS, and PVA@PCLS are shown in Figure 3h. The stretching vibration peak of the –OH bonds is in the range of 3200–3600 cm^{-1}. The stretching vibration of aliphatic ether bond (C–O–C) in PVA@CLS and PVA@PCLS can be indicated at 1092 cm^{-1}, showing that PVA and the LS-based biochar are chemically crosslinked in PVA@CLS and PVA@PCLS. Compared with PVA@LS, the intensity of the –OH bonds of PVA@CLS and PVA@PCLS decrease, indicating that the content of –OH in CLS and PCLS decreases after carbonization.

After the pyrolysis of biomass, C, H, O, S, and N are generally the most common elements of biochar. The elemental compositions of PVA@LS, PVA@CLS, and PVA@PCLS are also determined by an elemental analyzer, and the results are listed in Table 1. The N content of PVA@LS is 1.5 wt%, which comes from LS. After carbonization, most of the N atoms can be removed from LS, as well as O and H, so the contents of the C element in PVA@CLS and PVA@PCLS increase. Compared with PVA@CLS, the C content of PVA@PCLS is higher, indicating that the carbonization degree of PVA@PCLS is higher, which is due to the use of activator in the preparation of PCLS.

3.3 | Mechanical properties of carbon-based interfacial evaporation materials

The mechanical properties of PVA@LS, PVA@CLS, and PVA@PCLS were tested by a universal compressor under 80% compression strain. The compressive stress–strain curves of the three materials are shown in Figure 4a. At 80% deformation, the mechanical strength of PVA@LS, PVA@CLS, and PVA@PCLS can reach 12.94, 4.33, and 6.28 MPa, respectively. PVA@LS exhibits relatively better mechanical property than that of the PVA@CLS and PVA@PCLS. This can be attributed to LS having more functional groups and binding sites, thus forming a higher degree of crosslinking. There are fewer functional groups in PCLS, the addition of PCLS reduces the mechanical strength of PVA@PCLS.

To further vividly demonstrate the mechanical property of PVA@PCLS, a weight of 500 g (about 1177 times the weight of PVA@PCLS) was also placed on PVA@PCLS (Figure 4b), and then removed. It can be seen that the height of the PVA@PCLS block changes little before and after bearing and without any collapse, indicating the excellent mechanical strength of PVA@PCLS. As a result, though the mechanical strength of PVA@PCLS is less than that of PVA@LS, it still has excellent mechanical performance and can be applied to various scenarios of solar photothermal evaporation systems.

TABLE 1 Contents of C, H, O, S, N elements of PVA@LS, PVA@CLS, and PVA@PCLS.

Samples	C (wt%)	H (wt%)	O (wt%)	S (wt%)	N (wt%)
PVA@LS	58.5	4.5	29.9	5.6	1.5
PVA@CLS	72.1	3.2	23.3	1.0	0.4
PVA@PCLS	74.3	3.0	21.0	1.6	0.1

Abbreviations: LS, lignosulfonate; PCLS, porous LS-based biochar powder; PVA, polyvinyl alcohol.

3.4 | Water transport capacity of biochar-based interfacial evaporation materials

The hydrophilicity of aerogel evaporators is determined by the contact angle with water, whose PVA@LS, PVA@CLS, and PVA@PCLS evaporators are shown in Figure 5a. The results show that the three evaporators all have favorable hydrophilicity, which is conducive to water transport and steam overflow in the evaporation process. It can be seen from the figure that after 5 s, a drop of water (2 μL) can be absorbed in PVA@LS completely. On PVA@CLS and PVA@PCLS, the contact angles are 33° and 38°, revealing that PVA@CLS and PVA@PCLS are also suitable for water transport. The favorable hydrophilicity of the materials lays a foundation for the water transport competence in the process of photothermal evaporation.

Water transportation in the polymer gel can be also indicated by their swelling properties. The water transport in the internal gap and microchannel is realized by the capillarity, and the diffusion of water to the molecular grid depends on the permeation effect. The saturated water content is expressed by the weight of water per gram of dry gel in the fully swollen sample. As shown in Figure 5b, the saturated water content of PVA@LS, PVA@CLS, and PVA@PCLS are 6.21, 5.75, and 5.74 g/g, respectively. Since PVA@LS has more hydrophilic groups, its swelling rate is larger, which is also consistent with the results of the infrared test. On the other hand, a dynamic analysis of the swelling process is also conducted to evaluate the water transport rate in the interfacial evaporation material, which is expressed by the water absorption amount per minute. It can be seen that the water transport rate of PVA@LS, PVA@CLS, and PVA@PCLS are 0.06459, 0.05847, and 0.05392 g/min, respectively.

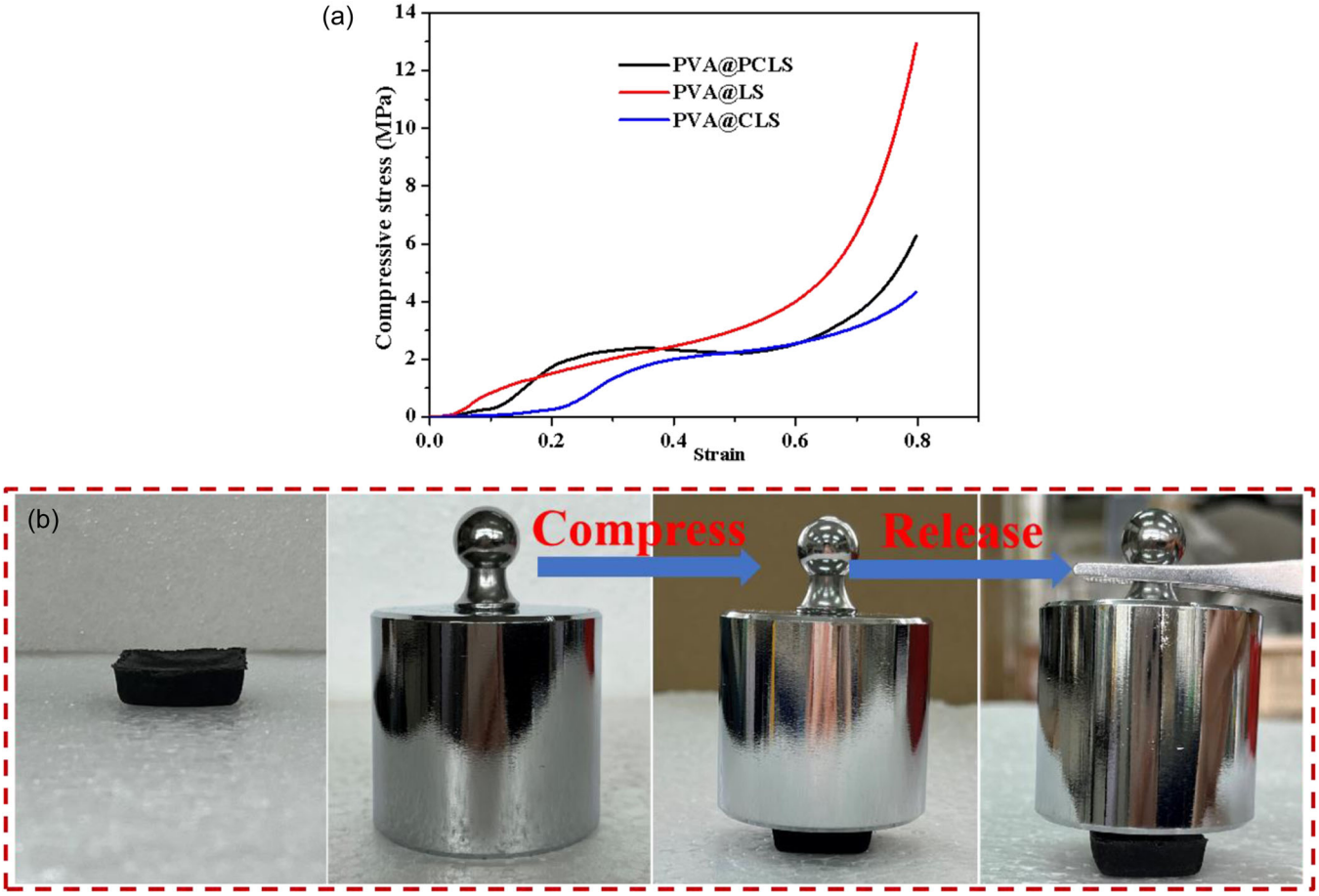

FIGURE 4 (a) Compressive stress–strain curves of PVA@LS, PVA@CLS, and PVA@PCLS; (b) PVA@PCLS with 500 g weight before and after bearing. LS, lignosulfonate; PCLS, porous LS-based biochar powder; PVA, polyvinyl alcohol.

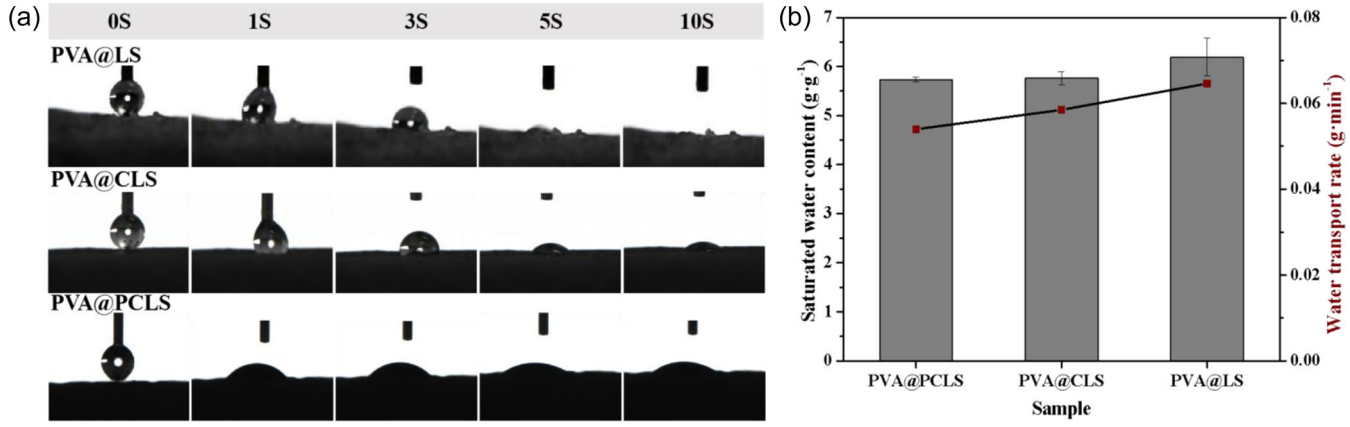

FIGURE 5 (a) The images of water contact angle on PVA@LS, PVA@CLS, and PVA@PCLS over time; (b) Saturated water content and water transport rate in PVA@LS, PVA@CLS, and PVA@PCLS. LS, lignosulfonate; PCLS, porous LS-based biochar powder; PVA, polyvinyl alcohol.

3.5 | Light absorption properties of biochar-based interfacial evaporation materials

The light absorption performance of interfacial evaporation materials is a significant property in the photothermal evaporation process. The stronger the solar absorption capacity of materials is, the better sunlight harvesting capability will be. Figure 6a shows the light absorption spectrum of PVA@LS, PVA@CLS, and PVA@PCLS in the spectral range of 250–2500 nm. Obviously, the light absorptance of PVA@LS in the

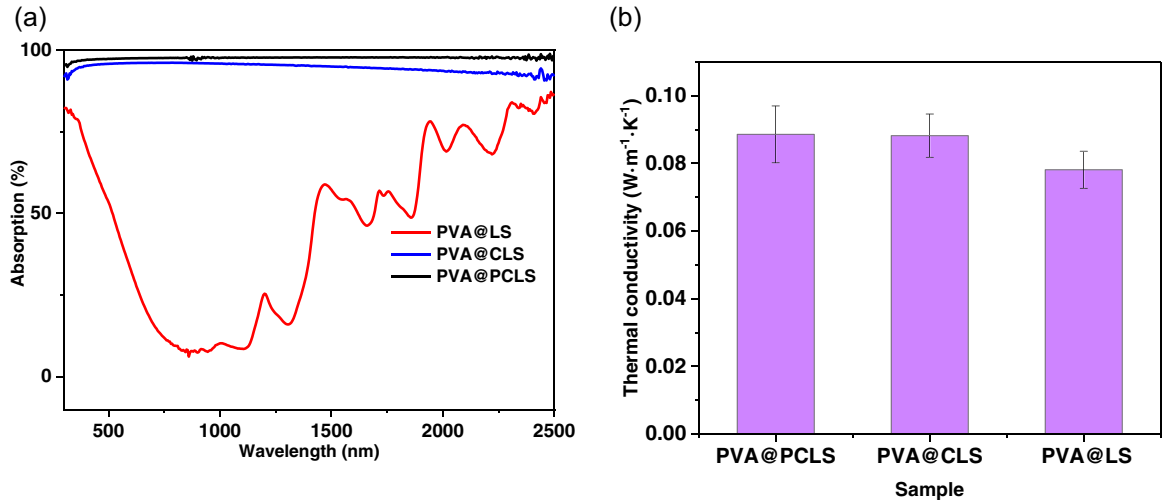

FIGURE 6 (a) Light absorption spectra of PVA@LS, PVA@CLS, and PVA@PCLS in the wavelength range of 250-2500 nm; (b) Thermal conductivity of PVA@LS, PVA@CLS and PVA@PCLS. LS, lignosulfonate; PCLS, porous LS-based biochar powder; PVA, polyvinyl alcohol.

full spectrum was weak (~33.26%), which is mainly due to the fact that original LS exhibits relatively low light adsorption. When PVA@CLS is synthesized after the carbonization of LS, the light absorption ability was significantly enhanced (~95.62%), which is due to the intrinsic high light absorption of carbon material. When synthesizing PVA@PCLS, the light absorption ability was further improved to 97.46%, because the particle size of PCLS was the smallest, which could attach to the surface of PVA and reduce light loss. At the same time, many multilevel pores are distributed inside the PCLS, which is conducive to the formation of optical traps to capture sunlight. When sunlight hits the material, it can create multiple scattering within the material, and get locked inside the material. Therefore, the optical absorbance of PVA@PCLS can increase the most.

The thermal conductivity of the aerogels under both dry and wet states at room temperature is measured and the results are shown in Figure 6b and Supporting Information: Figure S1. As shown in Figure 6b, the thermal conductivity of PVA@CLS and PVA@PCLS are 0.0882 and 0.0886 $W\,m^{-1}\,K^{-1}$ in dry condition, which is slightly higher than that of PVA@LS (0.0781 $W\,m^{-1}\,K^{-1}$). While in the wet state, the thermal conductivity of PVA@PCLS, PVA@CLS, and PVA@LS were measured to be 0.1851, 0.2311, and 0.2833 $W\,m^{-1}\,K^{-1}$. As we know, the thermal conductivity of water is 0.59 $W\,m^{-1}\,K^{-1}$ (25°C), while those of PVA@CLS and PVA@PCLS are much lower than that of water, suggesting that PVA@PCLS and PVA@CLS have good thermal insulation effect. In the process of photothermal evaporation, it can effectively reduce the heat loss of PVA@CLS and PVA@PCLS, during steam generation and facilitate the heat energy to concentrate on the surface of the material for photothermal conversion, thereby increasing the evaporation rate.

3.6 | Calculation of equivalent evaporation enthalpy of biochar-based interfacial evaporation materials

Two experiments are designed to determine the evaporation enthalpy of water in the polymer gel network. The first method is to determine the water evaporation rate and equivalent evaporation enthalpy in the dark condition. The results are shown in Figure 7a,b. The vaporization enthalpy of pure water is 2436 $J\,g^{-1}$, and the equivalent evaporation enthalpy in PVA@PCLS and PVA@CLS are 1436 and 1551 $J\,g^{-1}$.

The evaporation enthalpy is also tested by DSC test. Figure 7c is the DSC curves of pure water and water in the gel network. The weight loss curve of pure water decreases rapidly and reaches a maximum value (peak value), which is significantly different from that of water in the gel network. Compared with pure water, water in the gel network has shoulder peaks, showing that the evaporation process of pure water and water in the gel network are different. The hydrophilic groups (such as −OH) in the interfacial evaporation materials can bind with water through hydrogen bonds to form intermediate water (IW), thereby reducing the evaporation enthalpy of water, and thus effectively increasing the water evaporation rate.[31] The calculated evaporation enthalpy of pure water is 2337 $J\,g^{-1}$ (the theoretical value is 2436 $J\,g^{-1}$

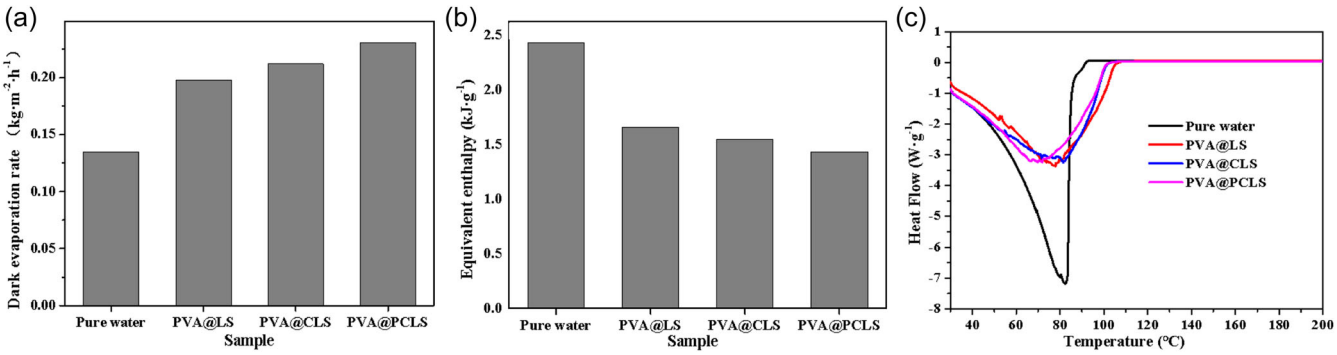

FIGURE 7 (a) Water evaporation rate in the dark condition; (b) The equivalent evaporation enthalpy of pure water and water in the gel network; (c) DSC curves of pure water and water in the gel network. DSC, differential scanning calorimetry.

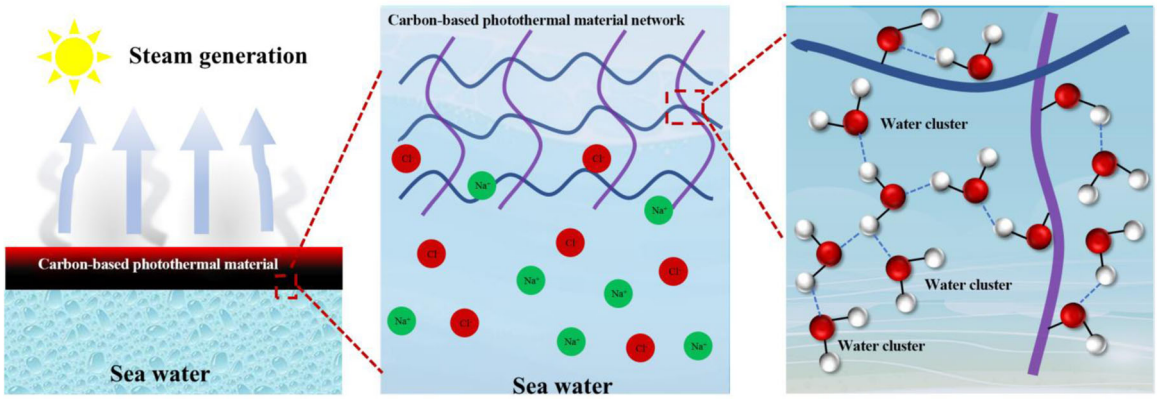

FIGURE 8 Schematic diagram of interfacial evaporation process.

[25°C]). The aerogel evaporators all showed lower vaporization enthalpy compared with pure water in the dark experiment as well as in the same trend with DSC results (Figure 7c).

The DSC measurement can only be used to qualitatively describe the reduction of evaporation enthalpy of water in the gel network. This is because DSC presents a full dehydration process of evaporators, which includes the energy requirement of vaporizing all three types of water (bound water [BW], IW, and free water [FW]). The more accurate evaporation enthalpy should only involve FW and IW. Dark experiment presents a slight dehydration, the subsequent calculation of the solar-to-vapor conversion efficiency will use the equivalent evaporation enthalpy obtained in the dark experiment.

To explain the decrease in evaporation enthalpy, Yu et al.[33–36] put forward a hypothesis that during the evaporation process, water molecules will form molecular clusters in the gel. These molecules are connected by intermolecular hydrogen bonds and form molecular clusters with the minimum energy through configuration changes (Figure 8). There exist three types of water molecules in the polymeric network, which can be categorized as FW (no interaction with polymer chains), IW (activation water with weak hydrogen bond between polymeric chains and surrounding water molecule), and BW (strong interaction with functional group of polymer chain). Some bounded clusters are activated to form IWs due to the hydrogen bond between the gel network and water molecules. During the evaporation process, these water clusters (i.e., IW) required the least energy to break intermolecular hydrogen bonds and escape from the liquid surface. As shown in Supporting Information: Figure S2, Raman spectroscopy was performed to measure the content of IW, these peaks can be classified into two types of modes of FW and IW. The measured value of IW/FW in PVA@PCLS was 1.01, which was higher than that of PVA@CLS (0.92). Moreover, the ratio of IW to FW in PVA@PCLS and PVA@CLS was greatly improved than that of pure water (0.39). The existence of IW could decrease the evaporation enthalpy and further reduce energy consumption of water vaporization. Therefore, the PVA@PCLS with the most IW, thus delivering the highest evaporation rate with the same energy input.

3.7 | Photothermal evaporation properties of biochar-based interfacial evaporation materials

To evaluate the photothermal conversion performance, steam evaporation experiments were conducted for three evaporators in the simulated sunlight with a light intensity of 1 kW m^{-2}. The temperature distribution on the dry surface of the three materials was recorded by infrared camera. Figure 9a is the infrared images, and Figure 9b is the temperature change curves. Under the light intensity of 1 kW m^{-2}, the surface temperature increases from room temperature to 31.5°C (PVA@LS), 37.3°C (PVA@CLS), and 43.8°C (PVA@PCLS) respectively after 15 s. After 6 min, the temperature reaches 41.2°C, 61.0°C, and 68.8°C, then the temperature rises to the highest value. After turning off the simulated sunlight, the temperature of the sample surface decreases rapidly. After 30 s, the surface temperature of PVA@LS, PVA@CLS, and PVA@PCLS decreases from the maximum temperature to 35°C, 48°C, and 44°C, respectively. The heat inside the sample quickly diffuses around the environment. After 3 min, the surface temperature of the material returns to room temperature. As can be seen from Figure 9b, the surface temperature of PVA@PCLS is higher than that of PVA@CLS at about 7°C. It means that when the carbon particles are smaller and have a porous structure, the photothermal performance is stronger, so does the light-to-heat conversion capacity, which is also consistent with the results of the light absorption test.

The mass change of water evaporation of the three materials under the simulated sunlight was tested. Figure 10a shows the relationship between the mass of water evaporation with time when different materials are used. There are obvious differences in the four curves. When the light intensity is 1 kW m^{-2}, the water evaporation rate of pure water is 0.506 kg m^{-2} h^{-1}, while that of PVA@LS, PVA@CLS, and PVA@PCLS are 1.03, 1.82, and 2.33 kg m^{-2} h^{-1}, respectively. Obviously, the evaporation rate of PVA@PCLS is higher by 4.6 times than that of pure water. The surface temperature of the materials in water was also recorded by the infrared camera during the experiment. Figure 10b displays the temperature curves under 1 kW m^{-2}. Figure 10c shows the infrared images of the material surface temperature during the photothermal evaporation process.

The results showed that the water evaporation rate and the solar-to-vapor conversion efficiency of PVA@PCLS are much greater than that of PVA@CLS and PVA@LS. There are two reasons for this phenomenon. First, amorphous carbon materials are formed after the carbonization of LS, and π–π^* transition occurs inside the material after absorbing photon energy, so these biochar-based materials have broadband absorption in the full spectrum.[37] Second, there are many graded channels inside PCLS, the smallest aperture can reach the nanometer level. In general, the higher the light absorption across the full spectrum (250–2500 nm) of a material, the higher the water evaporation rate.

According to the equivalent evaporation enthalpy of water in solar evaporators, the solar-to-vapor conversion efficiency of PVA@LS, PVA@CLS, and PVA@PCLS are 38.4%, 69.3%, and 83.7%, respectively under 1 sun irradiation (the evaporation rate of the material in the dark condition is considered in the calculation) (Figure 10d). The water evaporation rate and solar-to-vapor conversion efficiency of this work were compared with those of photothermal materials reported in previous literature, as shown in Table 2. The water

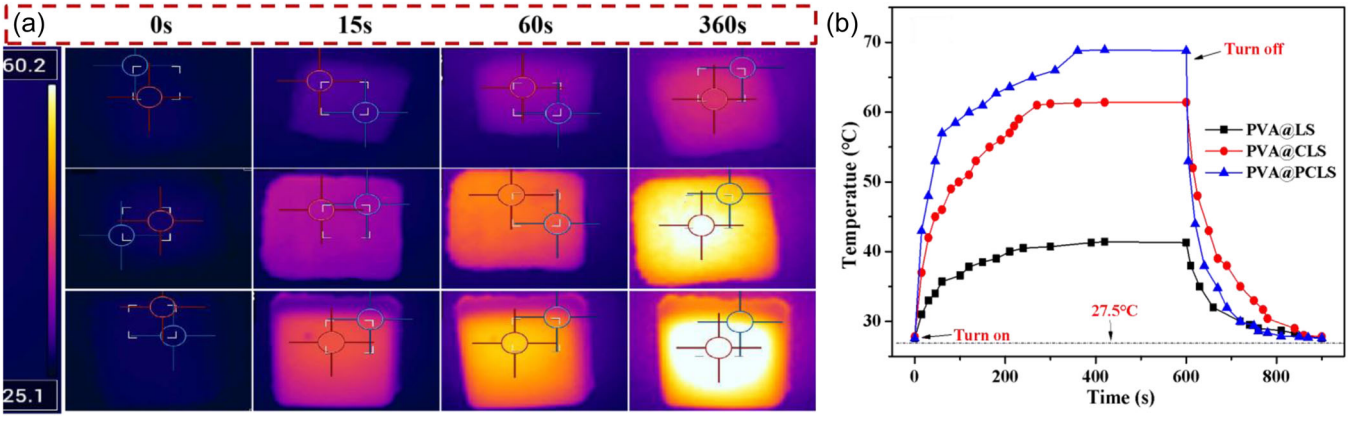

FIGURE 9 (a) Infrared images of surface temperature distribution of PVA@LS, PVA@CLS, and PVA@PCLS (dry state) at different time under 1 kW m^{-2}; (b) Surface temperature–time variation curves under 1 sun irradiation. LS, lignosulfonate; PCLS, porous LS-based biochar powder; PVA, polyvinyl alcohol.

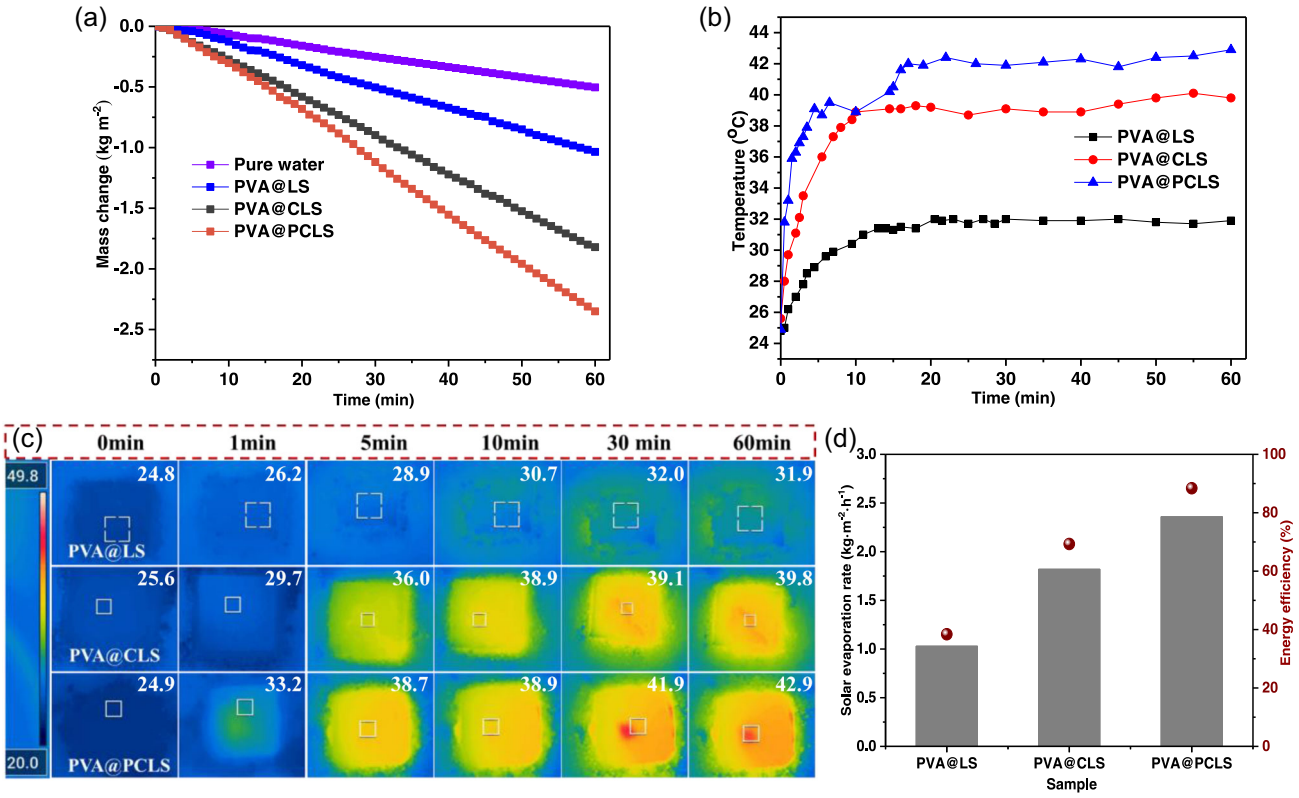

FIGURE 10 (a) The mass of water evaporation under 1 kW m^{-2}; (b) The surface temperature of PVA@LS, PVA@CLS, and PVA@PCLS relative to time under 1 kW m^{-2}; (c) The infrared images of the surface of PVA@LS, PVA@CLS and PVA@PCLS at different time under 1 kW m^{-2}; (d) The evaporation rate and solar-to-vapor conversion efficiency of PVA@LS, PVA@CLS, and PVA@PCLS under 1 kW m^{-2}. LS, lignosulfonate; PCLS, porous LS-based biochar powder; PVA, polyvinyl alcohol.

TABLE 2 Comparison of solar evaporation performance with PVA@PCLS and other evaporators.

Number	Reference	Solar evaporation rate (kg m^{-2} h^{-1})
1	Versatile chitosan aerogel[38]	1.57
2	Carbonized mushrooms[39]	1.48
3	Porous carbon @MnO_2[40]	1.72
4	Lignin hydrogel-based solar-driven evaporator[41]	2.25
5	Wood-derived aerogel[42]	1.35
6	Hydrogel-based solar evaporator[43]	2.60
7	Sugarcane-based photothermal materials[44]	1.59
This work	PVA@PCLS	2.33

Abbreviations: PCLS, porous LS-based biochar powder; PVA, polyvinyl alcohol.

evaporation capacity of PVA@PCLS is relatively higher than those of most reported biomass-based photothermal materials. In addition, the preparation process of PVA@PCLS is simple, which greatly reduces the preparation cost of water evaporation materials. The calculation of material cost is carried out for PVA@PCLS. The cost of the starting materials are listed in Table 3. From Table 3, it can be calculated that the cost of PVA@PCLS is $38.3/kg, which is far lower than other materials.[26] The low material cost means this material having an excellent application prospect in the field of photothermal evaporation.

In addition, the effects of different light intensities on the water evaporation rate of PVA@PCLS are also explored. The experimental results are shown in Figure 11a. The water evaporation rate increases with

TABLE 3 The cost of the starting materials for PVA@PCLS.

Materials	Grade	Price	Cost[a] ($/kg PVA@PCLS)
Sodium lignosulfonate	Industrial purity	$0.552/1000 g	0. 22
glutaraldehyde	Chemical purity	$8.69/500 mL	2.18
PVA	Chemical purity	$12.1/500 g	24.3
$CaCl_2$	Chemical purity	$5.38/500 g	4.30
K_2CO_3	Chemical purity	$4.97/500 g	5.97
HCL	Chemical purity	$0.552/500 mL	1.10

Abbreviations: PCLS, porous LS-based biochar powder; PVA, polyvinyl alcohol.

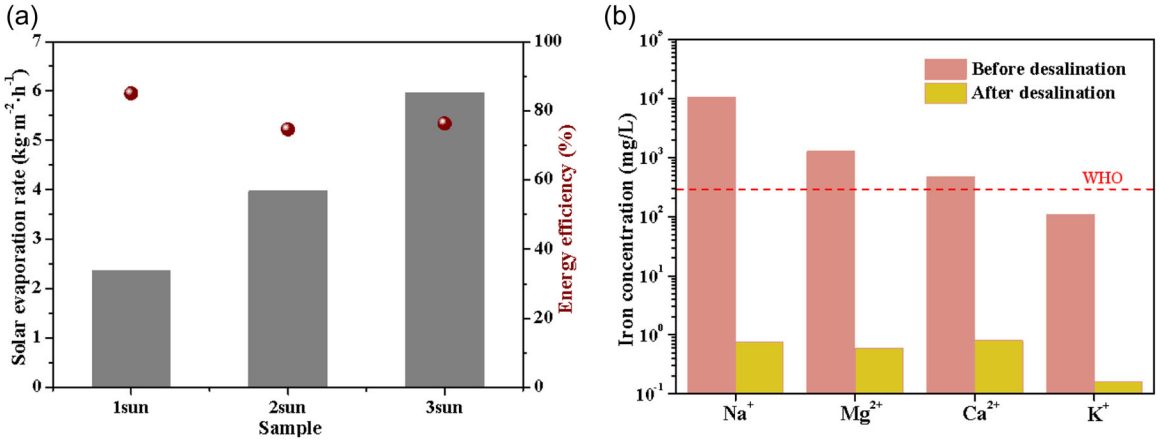

FIGURE 11 (a) The evaporation rate and solar-to-vapor conversion efficiency of PVA@PCLS under different light intensity; (b) Concentrations of ions in the simulated seawater solar evaporation by using PVA@PCLS. LS, lignosulfonate; PCLS, porous LS-based biochar powder; PVA, polyvinyl alcohol.

the increase of light intensity. Especially, the evaporation rates of PVA@PCLS are 2.33, 3.97, and 5.97 kg m^{-2} h^{-1} under 1–3 kW m^{-2}, and the corresponding solar-to-vapor conversion efficiency are 83.7%, 74.6%, and 76.3%. It suggests that the solar-to-vapor conversion efficiency decreases with increasing light intensity, so PVA@PCLS works better at 1 kW m^{-2}.

To assess the desalination performance of PVA@PCLS, simulated seawater is used for the solar desalination experiment. The water desalinated by PVA@PCLS is collected, and the contents of four primary ions Na^+, K^+, Ca^{2+}, and Mg^{2+} before and after desalination are analyzed. As shown in Figure 11b, the ion concentrations in the desalinated water were markedly reduced by three to four orders of magnitude than that of original simulated seawater, and the removal ratios of the four ions are all more than 99%. The concentration of these four ions after desalination meets the WHO standard for drinking water. It shows that PVA@PCLS has promising applications in the field of seawater desalination.

To further investigate the salt resistance behavior of PVA@PCLS, the brine evaporation tests with different NaCl concentrations (3.5, 7.0, 10.5, 20 wt%) were carried out under 1 sun illumination. Figure 12 shows the water evaporation curve of PVA@PCLS in different concentrations of salt solution. The evaporation rates of PVA@PCLS in solutions with salt concentrations of 3.5, 7, 10, and 20 wt% are 2.01, 1.91, 1.83, and 1.71 kg m^{-2} h^{-1}, respectively, which is lower than that in pure water (2.33 kg m^{-2} h^{-1}). The evaporation rate decreases slightly with the increase of salt concentration. To simulate the continuous evaporation in seawater, the solar desalination test was exposed in 3.5 wt% NaCl solution for 7 days. From Supporting Information: Figure S3, the evaporation rates were stabilized at ~2.0 kg m^{-2} h^{-1}. Notably, as can be seen in Figure 12b, 0.5 g NaCl on the surface of PVA@PCLS could be eliminated after 60 min under 1 sun irradiation, the excellent salt discharge performance also proves the salt tolerance property of PVA@PCLS. This is mainly due to the fact that good hydrophilicity and abundant interconnected channels of PVA@PCLS ensure the water

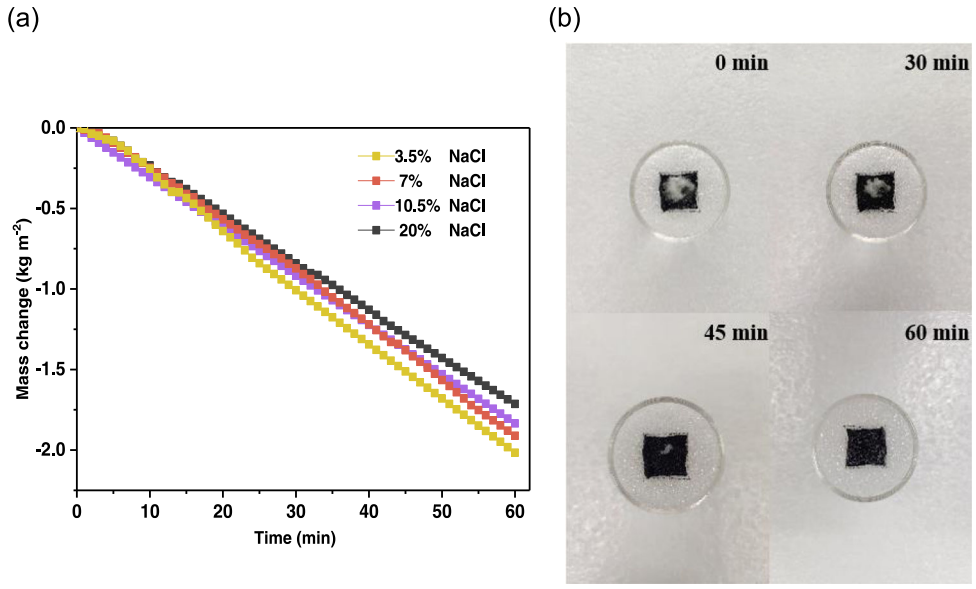

FIGURE 12 (a) Mass versus time curves of PVA@PCLS aerogels in NaCl solution with different concentrations under 1 kW m^{-2}; (b) Photographs showing the NaCl ablation process on the top surface of PVA@PCLS (1 sun). LS, lignosulfonate; PCLS, porous LS-based biochar powder; PVA, polyvinyl alcohol.

transport to the top surface of PVA@PCLS, thus preventing the salt crystallization. The above results indicate that the evaporator is perfectly capable of desalting seawater and can be applied in practical seawater purification.

4 | CONCLUSIONS

In this work, LS was carbonized as a solar absorber to fabricate interfacial evaporation materials. It is shown that the carbonization of LS can produce porous biochar in the presence of $CaCO_3$ as the activator. Among the three prepared interfacial evaporation materials, PVA@PCLS has the largest light adsorption, which is more than 97% in the full optical spectrum range. The compression strength of PVA@PCLS is 6.28 MPa, benefiting for the application in various scenarios of seawater desalination. Under the light intensity of 1 kW m^{-2}, the evaporation rate of PVA@PCLS is about 4.6 times larger than that of pure water, and the solar-to-vapor conversion efficiency is 83.7%. Various ion concentrations in freshwater generated by simulated seawater evaporation are well below WHO standards for drinking water. In summary, PVA@PCLS is a green photothermal evaporation material. This work extends high value-added utilization of biomass derivatives in solar steam generation.

AUTHORS CONTRIBUTIONS

Dafeng Zheng and Dongjie Yang completed conceptualization and supervision of the project. Lan Sun prepared the draft manuscript, completed methodology and investigation. Shilin Chen finished the characterization experiments and revised the mauscript. Yuqing Huang and Mingsong Zhou revised the manuscript. All authors reviewed the manuscript.

ACKNOWLEDGMENTS

The authors are very grateful to the National Key Research and Development Plan (2018YFB1501503), the Guangdong Natural Science Foundation (2022A1515010757), the National Natural Science Foundation of China (22178127) and the Science and Technology Program of Guangdong (2020B1111380002) to support this work.

CONFLICT OF INTEREST STATEMENT

The authors declare no conflicts of interest.

DATA AVAILABILITY STATEMENT

Data will be available on request from the authors.

REFERENCES

[1] M. Salehi, *Environ. Int.* **2022**, *158*, 106936.
[2] J. Bartram, C. Brocklehurst, M. Fisher, R. Luyendijk, R. Hossain, T. Wardlaw, B. Gordon, *Int. J. Environ. Res. Public Health* **2014**, *11*, 8137.
[3] K. Kim, S. Yu, C. An, S. W. Kim, J. H. Jang, *ACS Appl. Mater. Interfaces* **2018**, *10*, 15602.
[4] S. F. Anis, R. Hashaikeh, N. Hilal, *Desalination* **2019**, *468*, 114077.
[5] V. Davy, A. Lorenzo, F. Luc, *Sci. Rep.* **2022**, *12*, 3037.
[6] T. Li, H. Liu, X. Zhao, G. Chen, J. Dai, G. Pastel, C. Jia, C. Chen, E. Hitz, D. Siddhartha, R. Yang, L. Hu, *Adv. Funct. Mater.* **2018**, *28*, 1707134.
[7] V. D. Dao, N. H. Vu, S. Yun, *Nano Energy* **2020**, *68*, 104324.

[8] L. Zhu, M. Gao, C. K. N. Peh, G. W. Ho, *Mater. Horizons* **2018**, *5*, 323.
[9] C. Chen, Y. Kuang, L. Hu, *Joule* **2019**, *3*, 683.
[10] P. Zhang, Q. Liao, H. Yao, Y. Huang, H. Cheng, L. Qu, *Energy Storage Mater.* **2019**, *18*, 429.
[11] K. Garg, V. Khullar, S. K. Das, H. Tyagi, *Renew. Energy* **2018**, *122*, 140.
[12] Y. Li, T. Gao, Z. Yang, C. Chen, W. Luo, J. Song, E. Hitz, C. Jia, Y. Zhou, B. Liu, B. Yang, L. Hu, *Adv. Mater.* **2017**, *29*, 1700981.
[13] Q. Hou, C. Xue, N. Li, H. Wang, Q. Chang, H. Liu, J. Yang, S. Hu, *Carbon* **2019**, *149*, 556.
[14] M. Q. Yang, C. F. Tan, W. Lu, K. Zeng, G. W. Ho, *Adv. Funct. Mater.* **2020**, *30*, 2004460.
[15] B. Soo Joo, I. Soo Kim, I. Ki Han, H. Ko, J. Gu Kang, G. Kang, *Appl. Surf. Sci.* **2022**, *583*, 152563.
[16] H. Wang, L. Miao, S. Tanemura, *Solar RRL* **2017**, *1*, 1600023.
[17] G. Liu, T. Chen, J. Xu, G. Li, K. Wang, *J. Mater. Chem. A* **2020**, *8*, 513.
[18] D. Wu, C. Zhao, Y. Xu, X. Zhang, L. Yang, Y. Zhang, Z. Gao, Y. Y. Song, *ACS Appl. Nano Mater.* **2020**, *3*, 10895.
[19] T. Saito, R. H. Brown, M. A. Hunt, D. L. Pickel, J. M. Pickel, J. M. Messman, F. S. Baker, M. Keller, A. K. Naskar, *Green Chem.* **2012**, *14*, 3295.
[20] A. Tribot, G. Amer, M. Abdou Alio, H. de Baynast, C. Delattre, A. Pons, J. D. Mathias, J. M. Callois, C. Vial, P. Michaud, C. G. Dussap, *Eur. Polym. J.* **2019**, *112*, 228.
[21] J. Li, W. Liu, X. Qiu, X. Zhao, Z. Chen, M. Yan, Z. Fang, Z. Li, Z. Tu, J. Huang, *Green Chem.* **2022**, *24*, 823.
[22] A. Rahimi, A. Ulbrich, J. J. Coon, S. S. Stahl, *Nature* **2014**, *515*, 249.
[23] B. Zhang, D. Yang, X. Qiu, Y. Qian, H. Wang, C. Yi, D. Zhang, *Carbon* **2020**, *162*, 256.
[24] J. Wang, D. Fan, L. Zhang, D. Yang, X. Qiu, X. Lin, *Chem. Eng. J.* **2023**, *454*, 139789.
[25] S. Cao, Q. Jiang, X. Wu, D. Ghim, H. Gholami Derami, P. I. Chou, Y. S. Jun, S. Singamaneni, *J. Mater. Chem. A* **2019**, *7*, 24092.
[26] D. Liu, B. Shi, C. Wang, Z. Li, X. Wang, B. Xu, L. Qu, *Ceram. Int.* **2022**, *48*, 9157.
[27] L. Guo, D. Li, H. Lennholm, H. Zhai, M. Ek, *Cellulose* **2019**, *26*, 4853.
[28] Y. Xiong, C. Wang, H. Wang, Q. Yao, B. Fan, Y. Chen, Q. Sun, C. Jin, X. Xu, *J. Mater. Chem. A* **2017**, *5*, 5813.
[29] H. Geng, *Carbohydr. Polym.* **2018**, *196*, 289.
[30] K. Rong, J. Wei, Y. Wang, J. Liu, Z. A. Qiao, Y. Fang, S. Dong, *Green Chem.* **2021**, *23*, 6065.
[31] F. Zhao, X. Zhou, Y. Shi, X. Qian, M. Alexander, X. Zhao, S. Mendez, R. Yang, L. Qu, G. Yu, *Nat. Nanotechnol.* **2018**, *13*, 489.
[32] Z. Xie, J. Zhu, L. Zhang, *ACS Appl. Mater. Interfaces* **2021**, *13*, 9027.
[33] X. Zhou, F. Zhao, Y. Guo, Y. Zhang, G. Yu, *Energy Environ. Sci.* **2018**, *11*, 1985.
[34] X. Zhou, Y. Guo, F. Zhao, G. Yu, *Acc. Chem. Res.* **2019**, *52*, 3244.
[35] Y. Guo, X. Zhou, F. Zhao, J. Bae, B. Rosenberger, G. Yu, *ACS Nano* **2019**, *13*, 7913.
[36] A. M. Saleque, N. Nowshin, M. N. A. S. Ivan, S. Ahmed, Y. H. Tsang, *Solar RRL* **2022**, *6*, 2100986.
[37] Y. Lu, X. Wang, D. Fan, H. Yang, H. Xu, H. Min, X. Yang, *Sustain. Mater. Technol.* **2020**, *25*, e00180.
[38] Y. Gu, X. Mu, P. Wang, X. Wang, J. Liu, J. Shi, A. Wei, Y. Tian, G. Zhu, H. Xu, J. Zhou, L. Miao, *Nano Energy* **2020**, *74*, 104857.
[39] N. Xu, X. Hu, W. Xu, X. Li, L. Zhou, S. Zhu, J. Zhu, *Adv. Mater.* **2017**, *29*, 1606762.
[40] Y. Luan, Y. Huang, L. Wang, M. Li, R. Wang, B. Jiang, *J. Electroanal. Chem.* **2016**, *763*, 90.
[41] S. Jiang, Z. Zhang, T. Zhou, S. Duan, Z. Yang, Y. Ju, C. Jia, X. Lu, F. Chen, *Desalination* **2022**, *531*, 115706.
[42] Q. Zhang, L. Li, B. Jiang, H. Zhang, N. He, S. Yang, D. Tang, Y. Song, *ACS Appl. Mater. Interfaces* **2020**, *12*, 28179.
[43] Y. Guo, F. Zhao, X. Zhou, Z. Chen, G. Yu, *Nano Lett.* **2019**, *19*, 2530.
[44] C. Xiao, L. Chen, P. Mu, J. Jia, H. Sun, Z. Zhu, W. Liang, A. Li, *ChemistrySelect* **2019**, *4*, 7891.

SUPPORTING INFORMATION

Additional supporting information can be found online in the Supporting Information section at the end of this article.

How to cite this article: S. Chen, L. Sun, Y. Huang, D. Yang, M. Zhou, D. Zheng, *Carbon Neutralization* **2023**;*2*:494–509.
https://doi.org/10.1002/cnl2.79